Check for updates

Attenuation correction assisted automatic segmentation for assessing choroidal thickness and vasculature with swept-source OCT

HAO ZHOU,[1] ZHONGDI CHU,[1] QINQIN ZHANG,[1] YINING DAI,[1,2] GIOVANNI GREGORI,[3] PHILIP J. ROSENFELD,[3] AND RUIKANG K. WANG[1,4,*]

[1]*Department of Bioengineering, University of Washington, Seattle, WA 98105, USA*
[2]*Shanxi Eye Hospital, Taiyuan, Shanxi, China*
[3]*Department of Ophthalmology, Bascom Palmer Eye Institute, University of Miami Miller School of Medicine, Miami, FL 33136, USA*
[4]*Department of Ophthalmology, University of Washington, Seattle, WA 98105, USA*
*wangrk@uw.edu

Abstract: Swept source optical coherence tomography (SS-OCT) is being used more widely in clinical studies to investigate the choroid due to its deeper penetration under the retinal pigment epithelium and improved image quality compared with spectral domain OCT. However, automatic methods to reliably assess choroidal thickness and vasculature are still limited. This paper reports an approach that applies attenuation correction on SS-OCT structural scans to facilitate accurate automatic segmentation of the choroid and provides visualization of the choroidal vasculature without the necessity of OCT angiography. After attenuation correction, enhanced interlayer contrast at the choroidal-scleral interface was observed (from 0.13 ± 0.05 to 0.29 ± 0.10; $P < 0.001$). An algorithm that segmented the choroid from attenuation compensated B-scans achieved significantly higher accuracy when compared with an automated segmentation performed on regular OCT scans ($91.8 \pm 3.7\%$ vs.$74.5 \pm 8.0\%$; $P < 0.01$). After attenuation correction, *en face* images of choroidal vessels were achieved with fewer artifacts from retinal vessels. Measurements of mean choroidal thickness and vessel density showed high repeatability. The attenuation correction assisted segmentation of the choroid and visualization of the choroidal vasculature will be helpful in studying the quantitative changes that occur in a myriad of diseases involving the choroid such as age-related macular degeneration, polypoidal choroidal vasculopathy, pathologic myopia, central serous chorioretinopathy, and inflammatory eye conditions.

1. Introduction

The importance of the choroid in understanding a wide range of ocular diseases is gaining increasing attention by the ophthalmic imaging community, with a particular emphasis on the relationship between choroidal thickness and the choroidal vasculature [1]. The choroid plays a critical role in maintaining normal vision by supporting the metabolic exchange of photoreceptors, retinal pigment epithelium (RPE) and outer retina, by contributing to blood flow to the optic nerve, and by performing ocular thermoregulation [2–4]. Choroidal thickness measurements, either when measured from a foveal B-scan or from a three dimensional (3D) volume scan, have been reported to be useful in the investigation of ocular diseases [1,5–7]. Thicker choroidal measurements were observed in ocular diseases such as central serous chorioretinopathy [8], Vogt-Koyanagi-Harada disease [9], and macular telangiectasis type 2 [10], while thinner choroidal measurements were observed in myopic eyes, diabetic eyes, and eyes with age-related macular degeneration (AMD) [11–13]. The thickness of the choroid is thought to be a surrogate for choroidal blood flow, which accounts

for 85% of all ocular blood flow, the impairment of which is thought to be associated with numerous ocular diseases such as AMD, diabetic retinopathy and central serous chorioretinopathy [1,5]. Furthermore, choroidal thickness was previously found to have a clear relationship with the density of large choroidal vessels [1,14], and in one investigation, the presence of reticular pseudodrusen was associated with global choroidal thinning and a decrease in choroidal vascular density, which suggested an underlying choroidal vasculopathy [1]. Therefore, a technique to reliably assess choroidal thickness and the choroidal vasculature over a wide area of the choroid would greatly facilitate our ability to study the choroid and its vasculature in a wide range of ocular diseases.

Swept source optical coherence tomography (SS-OCT) is gaining increasing attention as a powerful imaging modality in ophthalmology for improved imaging of the choroid due to its better penetration into the choroid with less sensitivity roll-off compared with spectral domain OCT [15,16]. Traditional clinical imaging with technologies such as fundus autofluorescence imaging, fluorescein angiography (FA) and indocyanine green angiography (ICGA) do not provide depth-resolved quantitative information about the choroid. Moreover, FA and ICGA are invasive techniques that carry a small risk of significant adverse events [17,18]. In contrast, OCT is a non-invasive, fast imaging technique that provides cross-sectional images of eyes with high resolution. Moreover, SS-OCT is ideally suited for choroidal imaging due to the longer wavelength of its light source [15,16]. However, automated methods for visualizing and measuring the choroid and its vasculature are surprisingly limited.

Several approaches have been attempted to use OCT for 3D visualization and thickness measurements of choroidal structures. Enhanced depth imaging OCT (EDI-OCT) was developed to achieve better images of the choroid by moving the choroid closer to the zero delay line and averaging the scans [19,20]. However, the data acquisition took longer because it required multiple B-scans at a single position. Several methods followed to explore segmentation of the choroid and its vessels, however, they are either complicated and time-consuming or they require further refinement. For example, shadow compensation used Vupparaboina method to binarize images after compensating each pixel's intensity with a unique factor [21]. Seed-detection method applied multiscale Hessian matrix and calculated vessels using eigenvectors of the tensor matrix [22]; and edge filtering method performs multiscale edge filtering and calculated probability cones for each voxel [23]. Furthermore, choroid thickness measurement depends on the definition of posterior boundary at the outer border of choroidal vessels, the outer border of choroidal stroma or the inner border of the sclera [24,25]. The outer border of choroidal vessels is considered to be more clinically relevant since choroid is a vascular network [26]. Although SS-OCT achieves better imaging of the choroid, it is still difficult to distinguish the vessel boundaries at the choroidal-scleral interface (CSI) due to the shadows cast by retinal vessels and the attenuation of light with depth. Therefore, most of the automated segmentation methods developed to identify the choroidal boundary and the choroidal vessels were limited by the poor image contrast at the vessel boundaries and at the CSI [22,23,27–30]. While enhancement of the contrast at the CSI boundary has been applied to SD-OCT images with improved automated segmentation of choroid, the field-of-view under the macula was small [31].

The contrast of choroidal structures is low in the OCT images because light is progressively attenuated as it penetrates due to the scattering effect of biological tissues [32]. Particularly at the position of CSI boundaries, the OCT light beam must survive the strong light scattering of the RPE, the stroma tissue, and the blood within the lumens of choroidal vessels. To enhance the contrast of the CSI in the OCT image so as to facilitate the development of an automated segmentation algorithm for the accurate visualization and quantification of the choroidal information, we developed a strategy that mitigated this light attenuation effect in the OCT images. We focused on the optical attenuation coefficient (OAC) as one of the many physical parameters that can be extracted from OCT imaging as a function of the underlying tissue properties. Quantification of OAC from OCT data has been

shown to successfully identify atherosclerotic plaques [33], axillary lymph nodes [34] and cancerous tissues in the bladder [35]. In addition, it has been applied to the study of brain and skin and has shown enhanced resolution of structural tissue changes in damaged areas and facilitated automated segmentation strategies [36–38]. Previous studies also showed that this method improved the quality of OCT images, which enabled better segmentation of the optic nerve head [39]. However, attenuation correction has not yet been applied to choroidal segmentation with SS-OCT. Such a compensation method when applied to the dense tissues of the choroid combined with the attenuated signal that results from the RPE complex should provide enhanced contrast and help facilitate accurate segmentation.

Not only is choroidal boundary segmentation important, but choroidal vascular segmentation from OCT structural scans should be valuable as well. Large choroidal vessels appear dark in structural OCT images due to the highly forward scattering properties of blood, often characterized by an anisotropic factor, g [40,41]. As the g factor of blood is around 0.99, the majority of the photons scatter forward in blood vessels and only a few (~1%) photons scatter backwards in a fashion that can be picked up by the detector. Previously, an adaptive threshold method that classified image pixels based on signal intensities was utilized to segment choroidal vessels [29]. After attenuation correction, we expected the enhanced contrast in the OCT scans to yield vasculature images of higher quality for applying this adaptive threshold method. Visualization of the choroidal vasculature can be facilitated further by viewing OCT structural information with inverted contrast. If successful, such an approach would be clinically useful because angiography of larger vessels could be achieved with regular OCT scans, without needing OCT angiography (OCTA), a new vascular imaging technique that has recently been clinically impactful in ophthalmology [42–44].

In this report, we propose a novel yet practical approach to the automatic segmentation of the choroid by using light attenuation correction of the choroidal structures and then using the inverted SS-OCT structure scans to image the choroidal vasculature. This automated method provides accurate assessment of choroid thickness and the choroidal vasculature over a large area in three dimensions by using only conventional 12x12 mm OCT structure scans.

2. Method

2.1 Scanning protocol

Images were acquired as part of a prospective OCT study approved by the University of Washington institutional review board (IRB). IRB-approved consents were obtained from all subjects before scanning and the use of unidentified personal and medical information. All procedures adhered to the tenets of Declaration of Helsinki. The SS-OCT instrument (PlexElite, Carl Zeiss Meditec Inc.) had a central wavelength of 1050 nm, a bandwidth of 100 nm, a scanning rate of 100 kHz with an A-scan depth of 3.0 mm in tissue. The 12X12mm macular scans were obtained and centered on the fovea.

2.2 OCT signal attenuation correction

Attenuation correction consists of two algorithms to compensate for light attenuation and to enhance contrast [39]. In an SS-OCT system, the photocurrent of the interference between a light beam from a reference mirror and that from a sample of interest can be described by [45,46]:

$$I_i[k_m] = \frac{\rho}{2^i} S[k_m][R_R + R_S + 2\sqrt{R_R R_S} \cos(2k_m \Delta x + \varphi_i)] \tag{1}$$

where I_i is the sampled SS-OCT signal from the ith detector, k is the optical wavenumber, the acquired signal ideally has m values with evenly spaced wavenumbers $\{k_1, k_{2,...}, k_m\}$, ρ is the responsivity of the OCT detector, $S[k_m]$ is the sample illumination power, Δx is the

difference of pathlength between reference arm and sample arm, and R_R and R_S are the reflectivity of the reference arm and sample arm. The cross-correlation term $H[k_m]$ is derived from Eq. (1) as:

$$H[k_m] = \frac{1}{2}\rho S[k_m]\sqrt{R_R R_S}\cos(2k_m\Delta x) \tag{2}$$

The depth-reflectivity profile $D(z)$ can be obtained by a discrete inverse Fourier transform of Eq. (2) as:

$$D(z) = \sum_{k=1}^{M} H(k_m)e^{-2k_m z} \tag{3}$$

It should be noted that there is a limitation in Eqs. (1), (2) and (3), which is the assumption that light does not attenuate during propagation. To overcome this limitation, we modified the equation by taking light attenuation into account. When light penetrates a tissue sample, it attenuates through absorption when a small portion is converted to heat while the rest scatters. Assuming the local attenuation is only dependent on the local scattering and a constant fraction of the scattered light is retro-propagated in the direction of observation for each tissue layer, then the local attenuation of the light at the depth z is proportional to the local reflectivity (R) with a constant backscattering coefficient (α). Therefore, it modifies the OCT A-scan signal in Eq. (3) to a continuous form as:

$$D_A(z) = D(z)e^{-2\alpha\int_0^z D(u)du} \tag{4}$$

Comparing Eq. (3) and (4) shows that the standard SS-OCT post-processing does not provide the exact signal D, but instead its attenuated version, D_A. This is the major reason why shadows appear at strong attenuating tissues like blood vessels and pigments. To correct

the attenuation, the decay term $e^{-2\alpha\int_0^z D(u)du}$ needs be removed.

By integrating Eq. (4) on both sides, we have:

$$\int_z^\infty D_A(z)dz = \int_z^\infty D(z)e^{-2\alpha\int_0^z D(u)du}dz$$

$$= -\frac{1}{2\alpha}\int_z^\infty -2\alpha D(z)e^{-2\alpha\int_0^z D(u)du}dz = -\frac{1}{2\alpha}\left[e^{-2\alpha\int_0^z D(u)du}\right]_z^\infty \tag{5}$$

$$= \frac{e^{-2\alpha\int_0^z D(u)du}}{2\alpha}$$

After substituting Eq. (5) into Eq. (4):

$$D(z) = \frac{D_A(z)}{e^{-2\alpha\int_0^z D(u)du}} = \frac{D_A(z)}{2\alpha\int_z^\infty D_A(z)dz} \tag{6}$$

By discretizing Eq. (6), the OCT signals are compensated with attenuation correction at each pixel:

$$D(z) = \frac{D_A(z)}{2\alpha\sum_{z+1}^\infty D_A(z)} \approx \frac{D_A(z)}{2\alpha\sum_{z+1}^N D_A(z)} \tag{7}$$

where N is the final pixel in the A-scan and α can be adjusted according to tissue characteristics. This assumes that most of the light is attenuated within the recorded imaging depth [47].

Exponentiation on pixel intensities is a commonly applied method in image expansion for contrast enhancement purposes, such as in the commercial OCT systems. However, this exponentiation method is not optimal in regions with strong attenuation because such

transformation will show more shadows or, even worse, result in almost complete loss of signal [39]. This problem will no longer be a concern when coupled with attenuation correction. Therefore, exponentiation was applied before compensation in our approach and the overall pixel intensity is converted as:

$$D_{Attn-corr}(z) = \frac{D_A^2(z)}{2\sum_{z+1}^{N} D_A^2(z)} \tag{8}$$

where $D_{Attn-corr}$ is the signal after attenuation correction consisted of exponentiation and attenuation compensation. This algorithm reduces the heterogeneity of each layer and enhances the ability of edge detection between adjacent layers.
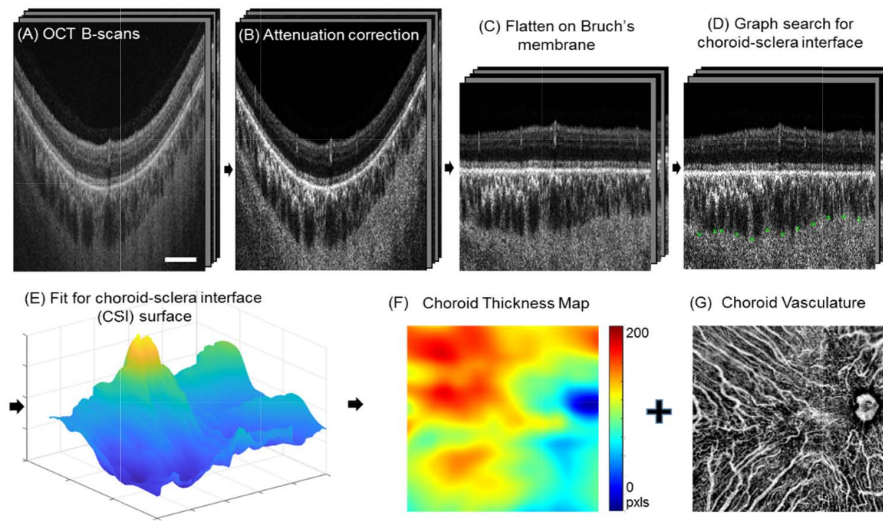

Fig. 1. Flow chart for attenuation correction assisted automatic segmentation of choroid and visualization of choroidal vasculature. Signals in regular OCT B-scans (A) were converted to OAC (B) with enhanced contrast. The image was flattened at Bruch's membrane that was fitted as the convex hull of the RPE bottom (C). Outer boundaries of the choroidal vessels were detected through a graph search (D) and were fitted for the choroidal-sclera interface via P-spline fitting (E). A choroidal thickness map (F) and vasculature map (G) were generated from the segmented choroidal slab. (Scale bar: 2 mm).

2.3 Automated segmentation of choroid

A choroid slab is segmented from Bruch's membrane to the CSI using a graph search method (Fig. 1(A)-1(E)). Here in this approach, we defined CSI as the outer border of choroidal vessels since it better represents the vascular nature of choroid [24–26]. In order to verify the improvement of attenuation correction on choroidal segmentation, we modified an automatic method that has been testified with a large number of normal data previously and demonstrated good performance on choroid segmentation of OCT scans without attenuation correction [27,30]. The open source software package can be found at https://www.mathworks.com/matlabcentral/fileexchange/61275-choroidsegmentation. We modified the algorithm in order to solve the fitting and quantification problem on the optical nerve head (ONH) in the 12mm x 12mm scanning region. Briefly, after attenuation correction (Fig. 1(B)), the region of optical nerve head is identified from the sum projection of the whole structure volume. A threshold of one standard deviation below the mean intensity of the whole *en face* projection was applied to segment the ONH. The region of ONH was excluded

in the detection of Bruch's membrane. Each B-scan was flattened at Bruch's membrane (Fig. 1(C)). Since the choroid consists of a network of vessels and the CSI is remarkably heterogeneous, the CSI is segmented via graph search edge detection for the minimum path across the bottoms of choroidal vessels [27]. After computing all the selected nodes for shortest path from each B-scan, the nodes at ONH region were assigned with thickness of zero. At last, we applied a P-spline method [44] to fit the surface of the CSI (Fig. 1(E)) since it works better to account for the irregular shape of ONH than the interpolation method used in the software package. The width of the B-splines was selected to be 50 pixels at both directions, penalties of 0.5 (out of 0~ + ∞) was applied on the neighboring coefficients of the tensor products at both directions. The weights for all the data points were all set to one. This method has been used previously to fit the shape of the macula [48,49]. Details are given in the Appendix of Ref. 48.

2.4 Enface mapping of choroidal thickness and vessels

A color-coded choroidal thickness map was generated to show the pixel distance between the locations of Bruch's membrane and the CSI at each A-Scan. Since large choroidal vessels appear to be dark in structural OCT images due to the highly forward scattering properties of blood [40], OCT signals with minimal intensities in the choroid slab indicate the position of choroid vessels. Therefore, choroidal vessel map was produced via minimum projection of OCT structural information using the automatically segmented choroid slab (Fig. 1(F)) and then inverted to present vessels as bright pixels. To do so, we ranked the enhanced OAC intensity values along the depth in the segmented choroid layer from smallest to largest and averaged the top 10% smallest values to produce the *en face* image Z.

We then invert and redistribute its histogram to adjust contrast (Fig. 1(G)) by:

$$Z'[x,y] = 255 - Z[x,y] \qquad (9)$$

and

$$Y = Y_{min} + \sqrt{2\beta^2 \ln(\frac{1}{1-P(Z')})} \qquad (10)$$

where Y is the output intensity, Y_{min} is the lower bound of the image, P is the cumulative probability of the input and β is the Rayleigh parameter. Histogram equalization increases the global contrast of the images [50].

2.5 Assessing interlayer contrast

In order to verify that the proposed attenuation correction can better facilitate accurate segmentation of choroid, the interlayer contrast (*IC*) across the CSI was computed before and after attenuation correction [39]. The interlayer contrast was defined as:

$$\text{Interlayer contrast}\,(\text{IC}) = \left| \frac{I_1 - I_2}{I_1 + I_2} \right| \qquad (11)$$

where I_1 and I_2 are the mean image intensities of a region of interest with 5 × 20 pixels (120 μm parallel along interface and 39 μm perpendicular to the interface) above and below the CSI. Ten random locations along the CSI were selected for *IC* calculation of each OCT B-scan. A larger interlayer contrast indicates a more detectable boundary.

3. Results

Five normal subjects were recruited for this study to demonstrate the proposed method (mean age: 48 ± 12 years, 3 males, 2 females). Attenuation correction significantly enhanced the *IC* at the CSI (from 0.13 ± 0.05 to 0.29 ± 0.10; P < 0.001), which provided more easily

detectable boundaries between choroid and sclera (Fig. 2(A)-2(C)). Unlike the retina which is almost transparent, the RPE, choroid and sclera are all scattering tissues that strongly attenuate incident light. Therefore, after attenuation correction, B-scans showed an enhanced contrast at the boundaries of these scattering tissues especially at the CSI. Because of this, the accuracy of automatic choroidal segmentation was largely improved. After applying the same procedures on the regular B-scans before attenuation correction, Fig. 2(D)-2(F) shows three adjacent B-scans where CSI segmentation was partially incorrect and variable. Some outer vessel boundaries were selected at Sattler's layer instead of Haller's layer due to the blurring of the CSI boundary. Figure 2(G)-2(I) shows that the CSI boundaries were successfully detected on the corresponding B-scans after attenuation correction and were consistent among adjacent B-scans.
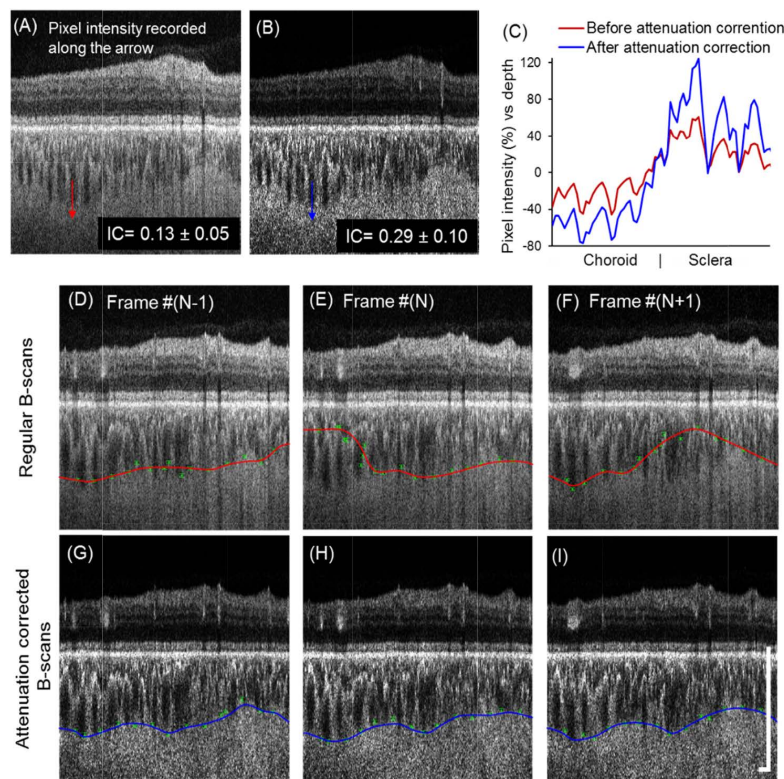

Fig. 2. Attenuation correction significantly enhanced the contrast of the CSI and the accuracy of the automatic CSI segmentation. (A-B) Interlayer contrast (IC) was significantly increased (P < 0.001) after attenuation correction. (C) Axial pixel intensity (percentage difference from mean) were recorded along the arrows. Attenuation correction improved the percentage difference in the axial pixel intensity at the CSI. (D-I) Automatic segmentations of the CSI for three adjacent B-scans before (D-F, red line) and after (G-I, blue line) attenuation correction are shown. Nodes of the outer choroidal vessel borders with corresponding weight (error bar) were labeled in green. CSI detected from regular OCT B-scans shows variability while the CSIs detected after attenuation correction were consistent and accurate. (Scale bar: 0.5 mm).

The automatic segmentations before and after attenuation correction were compared with manual segmentations on B-scans after attenuation correction from experienced graders. The mean choroid thickness from manual segmentations on B-scans before and after attenuation has been compared and showed no significant difference (P = 0.391, Paired Student's t-test). Accuracy of the automatic segmentation was obtained by comparing the agreement between

the automated segmentation method and the 'ground truth' (GT), which was defined as human annotation of the CSI on each B-scan after attenuation correction. Accuracy is calculated as the number of correctly segmented B scans over the total number of processed B-scans. Although P-spline fitting is capable of eliminating irregular nodes, it often fails if too many B-scans are segmented inaccurately. Other metrics such as correlation coefficient, absolute boundary difference (ABD), and overlap ratio were used to assess the differences between the final fitted automatic segmentations and the manual segmentations [28] (Table 1). The correlation coefficients, ABDs, and overlap ratios were similar to that of previously reported automatic segmentation methods [28]. All metrics showed that attenuation correction significantly improved the accuracy of automatic choroid segmentation (all P<0.05). Figure 3 (A)-3(C) show the thickness maps from different segmentation approaches on a normal eye. Automated segmentation of regular B-scans failed particularly at the macular region where the choroid is thick and OCT signal is weak (Fig. 3(D)-3(F), red line). After attenuation correction, the enhanced contrast at the CSI improved the accuracy of automatic segmentation (blue line) and there was a good match with the manual segmentations (white line).

Table 1. Accuracy, correlation coefficient, absolute boundary difference, and overlap ratios between manual segmentation and automatic segmentations before and after attenuation correction are shown. Data are represented as mean ± SD (n = 5); *, P<0.05; **, P< 0.01. Statistical analyses were conducted via paired T-test.

	Accuracy	Correlation coefficient	Absolute boundary difference	Overlap ratio
Automatic segmentation BEFORE attenuation correction	74.5 ± 8.0%	0.842 ± 0.088	24.7 ± 7.6 pxls	85.9 ± 5.6%
Automatic segmentation AFTER attenuation correction	91.8 ± 3.7%	0.973 ± 0.022	10.0 ± 5.9 pxls	93.7 ± 2.9%
P-value	0.002(**)	0.027(**)	0.006(**)	0.023(*)

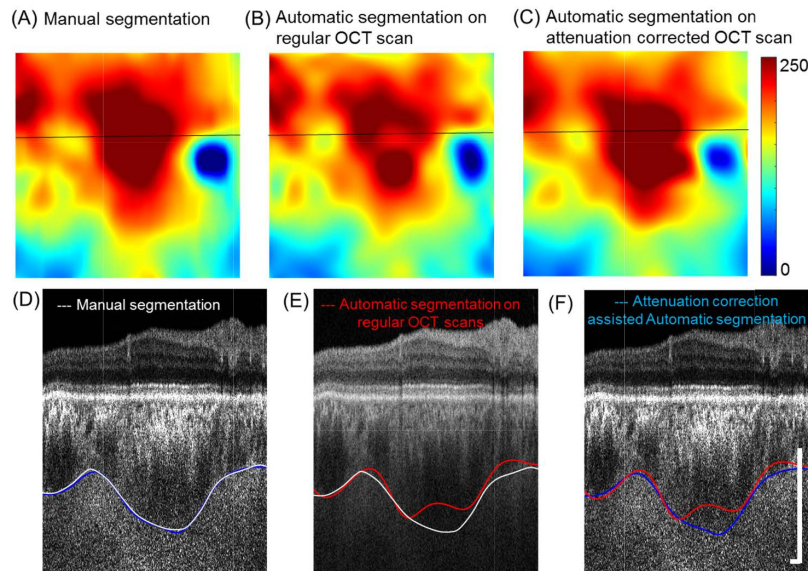Fig. 3. Segmentations of the choroid slabs were significantly more accurate after attenuation correction. (A-C) Choroid thickness maps of manual segmentation on B-scans after attenuation correction (A), automatic segmentation on regular OCT B-scans (B), and automatic segmentation of attenuation corrected OCT B-scans (C). (D-F) Corresponding B-scans (indicated by the black line on thickness maps) with manual segmentation (white line), and automatic segmentation before (red line) and after (blue line) attenuation correction. (Scale bar: 0.5 X 0.5 mm).

The other advantage of attenuation correction is that it eliminates shadows from large vessels after compensation for the attenuated light. Figure 4(A), 4(B) show representative B-scan with shadows from retina vessels before and after attenuation correction. From the lateral pixel intensity profile (Fig. 4(C)), we observed that the dark shadows had a much lower signal intensity before attenuation correction. Elimination of these shadows from retinal vessels is a critical step because choroidal vessel maps were produced via minimum projection of OCT structural information. Moreover, these shadows, which are dark in OCT structure scans, may be erroneously identified as choroidal vessels after being inverted. Attenuation correction successfully reduced these artifacts from retina vessels without any further processing being needed (Fig. 4(D)-4(F)). Choroidal vasculature area density of the entire scanning region is compared with and without attenuation correction and results showed that attenuation correction will significantly affected the choroidal vasculature area density (P<0.05, Paired Student's t-test) due to the elimination of shadows casted by retinal vessels.
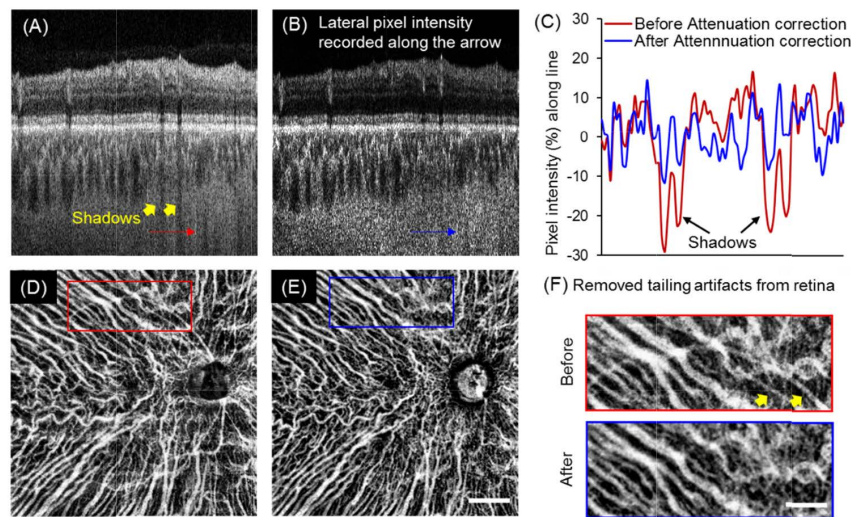

Fig. 4. Attenuation correction eliminated shadows from retinal vessels and largely reduced the artifacts when visualizing the choroidal vasculature. (A-B) Representative B-scan before and after attenuation correction. Shadows from retinal vessels shown with yellow arrows were markedly reduced after attenuation correction. (C) Lateral pixel intensity profiles along the shadows (indicated with red and blue arrows) showed the percentage difference from the mean intensities before and after attenuation correction. After attenuation correction, the indicated shadows were successfully eliminated. (D-E) Minimum projection of choroidal vessels of a normal eye without (D) and with (E) attenuation correction. (Scale bar: 2 mm). (F) Magnified regions (red and blue squares) of the vasculature showed the elimination of artifacts from the retina after attenuation correction. (Scale bar: 1 mm).

To validate our method and to test the repeatability of automatic choroidal segmentation and vasculature visualization assisted by attenuation correction, the mean choroid thickness (MT) and choroid vessel density (VD) measurements were calculated from four repeated scans from a normal eye. Excellent intra-visit repeatability of the choroidal thickness maps and vasculature patterns were observed (Fig. 5). MT is calculated as the mean value of the entire choroidal thickness map of 12x12 mm scanning region and VD is calculated as the area occupation percentage of choroidal vessels in the entire vasculature map excluding the ONH regions. The coefficient of correlation (CV) was calculated as $100 \times$ SD/mean. Measurements of MT and VD achieved CV% of $1.7 \pm 0.7\%$ and $0.41 \pm 0.18\%$ respectively, which indicated excellent repeatability for both measurements.
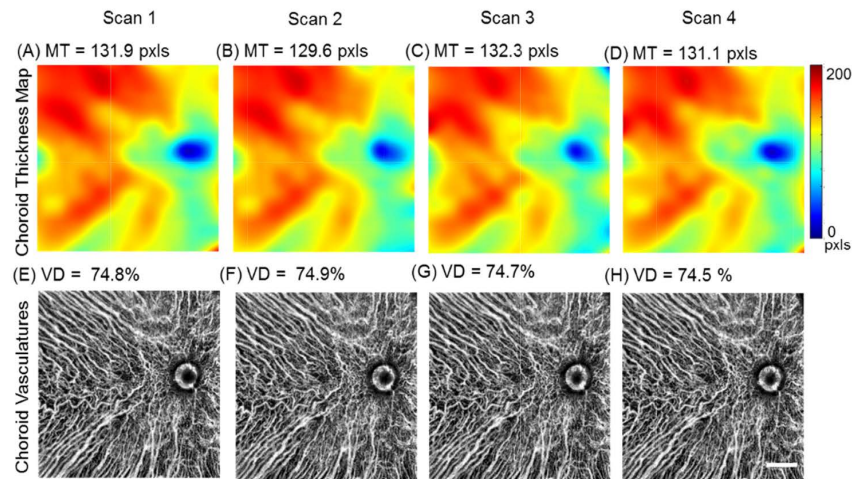
Fig. 5. Repeatability of attenuation correction assisted segmentation of the choroid and choroidal vasculature. Choroid thickness maps (A-D) and vasculature maps (E-H) of 4 repeated scans from a normal subject. MT = mean thickness. VD = vessel density. (Scale bar: 2 mm).

4. Discussions and conclusion

Overall, we have demonstrated an innovative and practical approach to achieve automated assessment of choroidal thickness and vascular density using attenuation correction of SS-OCT structural scans. Previous studies have validated the graphic search based automatic segmentation of choroid with 6x6 mm scanning regions under macular by SD-OCT and SS-OCT [51]. These automatic method is promising to achieve better performance with attenuation correction. While a single 3D OCT scan of 12x12 mm was used in this study to show the feasibility of the proposed method, it would be promising that when coupled with montage scanning protocols [52], non-invasive OCT structural imaging can provide comparable ultra-wide field-of-view choroidal vasculature imaging to that of ICGA, which is widely used in current clinic practice. The improved automated segmentation assisted by volumetric attenuation correction is also feasible to provide an ultra-wide field-of-view choroidal thickness map with improved accuracy. Choroidal thickness, either single sub-foveal B-scan measurements or three-dimensional volume measurements have been reported to be useful in investigating multiple ocular diseases [1,5–7]. Ultra-wide field-of-view choroidal thickness and vasculature maps could potentially bring added value to such investigations by covering larger regions of the posterior pole. We expect that attenuation correction assisted OCT imaging will provide real-time automated segmentation of the choroid and its vasculature, and when coupled with machine learning methods, this approach may enhance the use of choroidal pathology in diagnosing diseases.

In addition to mean thickness and vessel density, additional metrics such as stromal area, the area ratio of the choroidal stroma to vessels, and choroidal vessel tortuosity and complexity may serve as quantitative assessments to help understand diseases involving the choroid. These various quantitative evaluations of both choroidal structure and its vasculature may help scientists to better understand the morphology of choroid and its role in multiple ocular and systemic diseases.

Nonetheless, our method has several limitations. First of all, since the method of choroidal vessel visualization utilizes the dark appearance of choroidal vessels, which is essentially caused by the strong light scattering of the RPE complex [40,41], the resulting presentations of choroidal vessels is highly dependent on the healthy status of the RPE complex. If the RPE

complex is deteriorated, for example in geographic atrophy, then the method of extracting choroidal vessels may not work well. Secondly, since the light attenuation is not strong enough to cause the vessels in Sattler's layer to appear dark, the proposed method may not be able to reliably delineate the vessels in Sattler's layer. If the visualization of Sattler's layer is of interest, then one may consider coupling this method together with an OCTA technique to better assess the choroidal vasculature. Lastly, we have only tested the attenuation correction method with a limited number of subjects (n = 5). A further study with a larger sample size is required to validate the repeatability and reliability of the proposed method. A larger study is currently being conducted, including both normal and diseased eyes, and additional clinical applications will be reported in the future.

In summary, we have demonstrated that the enhanced contrast observed at the CSI after attenuation correction significantly increases the accuracy of automatic segmentation of the choroid. This enhancement and compensation method also eliminated shadow artifacts from retinal vessels, resulting in highly repeatable visualization and quantification of the vasculature. The importance of this outcome is that the real-time presentation of the choroidal thickness and its vasculature is feasible using conventional SS-OCT scans, does not require OCT angiographic capability, and can provide visualization of the choroidal vessels comparable to routine clinical ICGA imaging. The visualization of the choroidal vasculature and its structure and the ability to measure choroidal vessels and choroidal thickness will greatly facilitate our understanding of diseases that involve the choroid.

Disclosures

Dr. Gregori, Dr. Wang and Dr. Rosenfeld received research support from Carl Zeiss Meditec, Inc. Dr. Gregori and the University of Miami co-own a patent that is licensed to Carl Zeiss Meditec, Inc.

Dr. Rosenfeld also received additional research support from Genentech. He is a consultant for Achillion Pharmaceuticals, Acucela, Boehringer-Ingelheim, Carl Zeiss Meditec, Chengdu Kanghong Biotech, Ocunexus Therapeutics, Genentech, Healios K.K, Hemera Biosciences, F. Hoffmann-La Roche Ltd., Isarna Pharmaceuticals, Lin Bioscience, MacRegen Inc, NGM Biopharmaceuticals, Ocunexus,Ocudyne, Tyrogenex, and Unity Biotechnology. Dr. Rosenfeld has equity interest in Apellis, Digisight, and Ocudyne.

Dr. Wang discloses intellectual property owned by the Oregon Health and Science University and the University of Washington. Dr. Wang also receives research support from Tasso Inc, Moptim Inc, and Colgate Palmolive Company. He is a consultant to Insight Photonic Solutions, Kowa, and Carl Zeiss Meditec.

Dr. Zhou, Dr. Zhang, Dr. Dai and Ms. Chu have no disclosures.

References

1. F. Zheng, G. Gregori, K. B. Schaal, A. D. Legarreta, A. R. Miller, L. Roisman, W. J. Feuer, and P. J. Rosenfeld, "Choroidal thickness and choroidal vessel density in nonexudative age-related macular degeneration using swept-source optical coherence tomography imaging," Invest. Ophthalmol. Vis. Sci. **57**(14), 6256–6264 (2016).
2. R. A. Linsenmeier and L. Padnick-Silver, "Metabolic dependence of photoreceptors on the choroid in the normal and detached retina," Invest. Ophthalmol. Vis. Sci. **41**(10), 3117–3123 (2000).
3. S. S. Hayreh, "Blood supply of the optic nerve head and its role in optic atrophy, glaucoma, and oedema of the optic disc," Br. J. Ophthalmol. **53**(11), 721–748 (1969).
4. L. M. Parver, C. Auker, and D. O. Carpenter, "Choroidal Blood Flow as a Heat Dissipating Mechanism in the Macula," Am. J. Ophthalmol. **89**(5), 641–646 (1980).
5. P. Haas, M. Esmaeelpour, S. Ansari-Shahrezaei, W. Drexler, and S. Binder, "Choroidal thickness in patients with reticular pseudodrusen using 3D 1060-nm OCT maps," Invest. Ophthalmol. Vis. Sci. **55**(4), 2674–2681 (2014).
6. S. E. Chung, S. W. Kang, J. H. Lee, and Y. T. Kim, "Choroidal Thickness in Polypoidal Choroidal Vasculopathy and Exudative Age-Related Macular Degeneration," Ophthalmology **118**(5), 840–845 (2011).
7. I. Maruko, T. Iida, Y. Sugano, A. Ojima, M. Ogasawara, and R. F. Spaide, "Subfoveal Choroidal Thickness after Treatment of Central Serous Chorioretinopathy," Ophthalmology **117**(9), 1792–1799 (2010).
8. Y. Imamura, T. Fujiwara, R. Margolis, and R. F. Spaide, "Enhanced Depth Imaging Optical Coherence Tomography of the Choroid in Central Serous Chorioretinopathy," Retina **29**(10), 1469–1473 (2009).
9. I. Maruko, T. Iida, Y. Sugano, S. Go, and T. Sekiryu, "Subfoveal Choroid Thickness in Papillitis Type of Vogt-Koyanagi-Harada Disease and Idiopathic Optic Neuritis," Retina **36**(5), 992–999 (2016).
10. R. P. Nunes, R. Goldhardt, C. A. de Amorim Garcia Filho, M. R. Thorell, A. M. Abbey, A. E. Kuriyan, Y. S. Modi, M. Shah, Z. Yehoshua, G. Gregori, W. Feuer, and P. J. Rosenfeld, "Spectral-Domain Optical Coherence Tomography Measurements of Choroidal Thickness and Outer Retinal Disruption in Macular Telangiectasia Type 2," Ophthalmic Surg. Lasers Imaging Retina **46**(2), 162–170 (2015).
11. H. Ohsugi, Y. Ikuno, K. Oshima, and H. Tabuchi, "3-D Choroidal Thickness Maps from EDI-OCT in Highly Myopic Eyes," Optom. Vis. Sci. **90**(6), 599–606 (2013).
12. S. Kase, H. Endo, M. Yokoi, M. Kotani, S. Katsuta, M. Takahashi, and M. Kase, "Choroidal thickness in diabetic retinopathy in relation to long-term systemic treatments for diabetes mellitus," Eur. J. Ophthalmol. **26**(2), 158–162 (2016).
13. M. R. Thorell, R. Goldhardt, R. P. Nunes, C. A. de Amorim Garcia Filho, A. M. Abbey, A. E. Kuriyan, Y. S. Modi, G. Gregori, Z. Yehoshua, W. Feuer, S. Sadda, and P. J. Rosenfeld, "Association Between Subfoveal Choroidal Thickness, Reticular Pseudodrusen, and Geographic Atrophy in Age-Related Macular Degeneration," Ophthalmic Surg. Lasers Imaging Retina **46**(5), 513–521 (2015).
14. J. C. Wang, I. Laíns, J. Providência, G. W. Armstrong, A. R. Santos, P. Gil, J. Gil, K. E. Talcott, J. H. Marques, J. Figueira, D. G. Vavvas, I. K. Kim, J. W. Miller, D. Husain, R. Silva, and J. B. Miller, "Diabetic Choroidopathy: Choroidal Vascular Density and Volume in Diabetic Retinopathy With Swept-Source Optical Coherence Tomography," Am. J. Ophthalmol. **184**, 75–83 (2017).
15. A. R. Miller, L. Roisman, Q. Zhang, F. Zheng, J. Rafael de Oliveira Dias, Z. Yehoshua, K. B. Schaal, W. Feuer, G. Gregori, Z. Chu, C. L. Chen, S. Kubach, L. An, P. F. Stetson, M. K. Durbin, R. K. K. Wang, and P. J. Rosenfeld, "Comparison Between Spectral-Domain and Swept-Source Optical Coherence Tomography Angiographic Imaging of Choroidal Neovascularization," Invest. Ophthalmol. Vis. Sci. **58**(3), 1499–1505 (2017).
16. A. I. Dastiridou, E. Bousquet, L. Kuehlewein, T. Tepelus, D. Monnet, S. Salah, A. Brezin, and S. R. Sadda, "Choroidal Imaging with Swept-Source Optical Coherence Tomography in Patients with Birdshot Chorioretinopathy: Choroidal Reflectivity and Thickness," Ophthalmology **124**(8), 1186–1195 (2017).
17. L. A. Yannuzzi, K. T. Rohrer, L. J. Tindel, R. S. Sobel, M. A. Costanza, W. Shields, and E. Zang, "Fluorescein angiography complication survey," Ophthalmology **93**(5), 611–617 (1986).
18. M. A. Bloome, "Fluorescein angiography: risks," Vision Res. **20**(12), 1083–1097 (1980).
19. R. Margolis and R. F. Spaide, "A Pilot Study of Enhanced Depth Imaging Optical Coherence Tomography of the Choroid in Normal Eyes," Am. J. Ophthalmol. **147**(5), 811–815 (2009).
20. R. F. Spaide, H. Koizumi, and M. C. Pozzoni, "Enhanced depth imaging spectral-domain optical coherence tomography," Am. J. Ophthalmol. **146**(4), 496–500 (2008).
21. K. K. Vupparaboina, K. K. Dansingani, A. Goud, M. A. Rasheed, F. Jawed, S. Jana, A. Richhariya, B. K. Freund, and J. Chhablani, "Quantitative shadow compensated optical coherence tomography of choroidal vasculature," Sci. Rep. **8**, 6461 (2018).
22. L. Zhang, K. Lee, M. Niemeijer, R. F. Mullins, M. Sonka, and M. D. Abràmoff, "Automated Segmentation of the Choroid from Clinical SD-OCT," Invest. Ophthalmol. Vis. Sci. **53**(12), 7510–7519 (2012).
23. V. Kajić, M. Esmaeelpour, C. Glittenberg, M. F. Kraus, J. Honegger, R. Othara, S. Binder, J. G. Fujimoto, and W. Drexler, "Automated three-dimensional choroidal vessel segmentation of 3D 1060 nm OCT retinal data," Biomed. Opt. Express **4**(1), 134–150 (2013).
24. V. S. Vuong, E. Moisseiev, D. Cunefare, S. Farsiu, A. Moshiri, and G. Yiu, "Repeatability of Choroidal Thickness Measurements on Enhanced Depth Imaging Optical Coherence Tomography Using Different Posterior Boundaries," Am. J. Ophthalmol. **169**, 104–112 (2016).

25. G. Yiu, P. Pecen, N. Sarin, S. J. Chiu, S. Farsiu, P. Mruthyunjaya, and C. A. Toth, "Characterization of the Choroid-Scleral Junction and Suprachoroidal Layer in Healthy Individuals on Enhanced-Depth Imaging Optical Coherence Tomography," JAMA Ophthalmol. **132**(2), 174–181 (2014).

26. E. Huynh, E. Chandrasekera, D. Bukowska, S. McLenachan, D. A. Mackey, and F. K. Chen, "Past, Present, and Future Concepts of the Choroidal Scleral Interface Morphology on Optical Coherence Tomography," Asia Pac. J. Ophthalmol. (Phila.) **6**(1), 94–103 (2017).

27. L. Beaton, J. Mazzaferri, F. Lalonde, M. Hidalgo-Aguirre, D. Descovich, M. R. Lesk, and S. Costantino, "Non-invasive measurement of choroidal volume change and ocular rigidity through automated segmentation of high-speed OCT imaging," Biomed. Opt. Express **6**(5), 1694–1706 (2015).

28. Q. Chen, W. Fan, S. Niu, J. Shi, H. Shen, and S. Yuan, "Automated choroid segmentation based on gradual intensity distance in HD-OCT images," Opt. Express **23**(7), 8974–8994 (2015).

29. L. Duan, Y. J. Hong, and Y. Yasuno, "Automated segmentation and characterization of choroidal vessels in high-penetration optical coherence tomography," Opt. Express **21**(13), 15787–15808 (2013).

30. J. Mazzaferri, L. Beaton, G. Hounye, D. N. Sayah, and S. Costantino, "Open-source algorithm for automatic choroid segmentation of OCT volume reconstructions," Sci. Rep. **7**, 42112 (2017).

31. D. Alonso-Caneiro, S. A. Read, and M. J. Collins, "Automatic segmentation of choroidal thickness in optical coherence tomography," Biomed. Opt. Express **4**(12), 2795–2812 (2013).

32. R. K. Wang, "Signal degradation by coherence tomography multiple scattering in optical of dense tissue: a Monte Carlo study towards optical clearing of biotissues," Phys. Med. Biol. **47**, 2281–2299 (2002).

33. C. Xu, J. M. Schmitt, S. G. Carlier, and R. Virmani, "Characterization of atherosclerosis plaques by measuring both backscattering and attenuation coefficients in optical coherence tomography," J. Biomed. Opt. **13**(3), 034003 (2008).

34. L. Scolaro, R. A. McLaughlin, B. R. Klyen, B. A. Wood, P. D. Robbins, C. M. Saunders, S. L. Jacques, and D. D. Sampson, "Parametric imaging of the local attenuation coefficient in human axillary lymph nodes assessed using optical coherence tomography," Biomed. Opt. Express **3**(2), 366–379 (2012).

35. E. C. C. Cauberg, D. M. de Bruin, D. J. Faber, T. M. de Reijke, M. Visser, J. J. M. C. H. de la Rosette, and T. G. van Leeuwen, "Quantitative measurement of attenuation coefficients of bladder biopsies using optical coherence tomography for grading urothelial carcinoma of the bladder," J. Biomed. Opt. **15**(6), 066013 (2010).

36. U. Baran, Y. Li, and R. K. Wang, "In vivo tissue injury mapping using optical coherence tomography based methods," Appl. Opt. **54**(21), 6448–6453 (2015).

37. U. Baran, W. Zhu, W. J. Choi, M. Omori, W. Zhang, N. J. Alkayed, and R. K. K. Wang, "Automated segmentation and enhancement of optical coherence tomography-acquired images of rodent brain," J. Neurosci. Methods **270**, 132–137 (2016).

38. U. Baran, W. Qin, X. L. Qi, G. Kalkan, and R. K. Wang, "OCT-based label-free in vivo lymphangiography within human skin and areola," Sci. Rep. **6**, 21122 (2016).

39. M. J. A. Girard, N. G. Strouthidis, C. R. Ethier, and J. M. Mari, "Shadow Removal and Contrast Enhancement in Optical Coherence Tomography Images of the Human Optic Nerve Head," Invest. Ophthalmol. Vis. Sci. **52**(10), 7738–7748 (2011).

40. M. A. Kirby, C. Li, W. J. Choi, G. Gregori, P. Rosenfeld, and R. Wang, "Why choroid vessels appear dark in clinical OCT images," in *Ophthalmic Technologies XXVIII*, (International Society for Optics and Photonics, 2018), 1047428.

41. R. K. K. Wang, M. Kirby, C. X. Li, W. J. Choi, G. Gregori, and P. J. Rosenfeld, "An explanation for why choroidal blood vessels appear dark on clinical OCT images," Invest. Ophthalmol. Vis. Sci. **58**, 4754 (2017).

42. L. An and R. K. K. Wang, "In vivo volumetric imaging of vascular perfusion within human retina and choroids with optical micro-angiography," Opt. Express **16**(15), 11438–11452 (2008).

43. C. L. Chen and R. K. Wang, "Optical coherence tomography based angiography [Invited]," Biomed. Opt. Express **8**(2), 1056–1082 (2017).

44. A. H. Kashani, C. L. Chen, J. K. Gahm, F. Zheng, G. M. Richter, P. J. Rosenfeld, Y. Shi, and R. K. K. Wang, "Optical coherence tomography angiography: A comprehensive review of current methods and clinical applications," Prog. Retin. Eye Res. **60**, 66–100 (2017).

45. P. H. Tomlins and R. K. Wang, "Theory, developments and applications of optical coherence tomography," J. Phys. D Appl. Phys. **38**(15), 2519–2535 (2005).

46. M. Choma, M. Sarunic, C. Yang, and J. Izatt, "Sensitivity advantage of swept source and Fourier domain optical coherence tomography," Opt. Express **11**(18), 2183–2189 (2003).

47. K. A. Vermeer, J. Mo, J. J. A. Weda, H. G. Lemij, and J. F. de Boer, "Depth-resolved model-based reconstruction of attenuation coefficients in optical coherence tomography," Biomed. Opt. Express **5**(1), 322–337 (2014).

48. R. W. Knighton and G. Gregori, "The Shape of the Ganglion Cell plus Inner Plexiform Layers of the Normal Human Macula," Invest. Ophthalmol. Vis. Sci. **53**(11), 7412–7420 (2012).

49. P. H. C. Eilers, I. D. Currie, and M. Durban, "Fast and compact smoothing on large multidimensional grids," Comput. Stat. Data Anal. **50**(1), 61–76 (2006).

50. S. M. Pizer, E. P. Amburn, J. D. Austin, R. Cromartie, A. Geselowitz, T. Greer, B. Terhaarromeny, J. B. Zimmerman, and K. Zuiderveld, "Adaptive Histogram Equalization and Its Variations," Comput Vision Graph **39**(3), 355–368 (1987).

51. L. Zhang, G. H. S. Buitendijk, K. Lee, M. Sonka, H. Springelkamp, A. Hofman, J. R. Vingerling, R. F. Mullins, C. C. W. Klaver, and M. D. Abràmoff, "Validity of Automated Choroidal Segmentation in SS-OCT and SD-OCT," Invest. Ophthalmol. Vis. Sci. **56**(5), 3202–3211 (2015).
52. Q. Q. Zhang, C. S. Lee, J. Chao, C. L. Chen, T. Zhang, U. Sharma, A. Q. Zhang, J. Liu, K. Rezaei, K. L. Pepple, R. Munsen, J. Kinyoun, M. Johnstone, R. N. Van Gelder, and R. K. K. Wang, "Wide-field optical coherence tomography based microangiography for retinal imaging," Sci. Rep. **6**, 22017 (2016).